Journal of Solid State Chemistry **147,** 99–116 (1999)
Article ID jssc.1999.8183, available online at http://www.idealibrary.com on IDEAL®

Structural Studies and Order–Disorder Phenomenon in a Series of New Quaternary Tellurates of the Type $A^{2+}M^{4+}\mathrm{Te}^{6+}\mathrm{O}_6$ and $A_2^{1+}M^{4+}\mathrm{Te}^{6+}\mathrm{O}_6$

Patrick M. Woodward[1]

Physics Department, Brookhaven National Laboratory, Upton, New York 11973

Arthur W. Sleight

Department of Chemistry, Oregon State University, Corvallis, Oregon 97331

and

Lin-Shu Du and Clare P. Grey

Department of Chemistry, State University of New York, Stony Brook, New York 11794-3400

Received October 12, 1998; accepted January 22, 1999

Five new compounds in the $A_xM\mathrm{TeO}_6$ family were prepared and structurally characterized: Li_2GeTeO_6, Na_2TiTeO_6, Na_2SnTeO_6, and two forms of Na_2GeTeO_6. All compounds are layered structures based on various stacking arrangements of $M\mathrm{TeO}_6^{2-}$ layers. The structures of $BaGeTeO_6$ and $SrGeTeO_6$ were also determined. The former compound was found to contain Ba^{2+} in trigonal prismatic coordination, in agreement with previous literature reports, while $SrGeTeO_6$ contains Sr^{2+} in octahedral coordination and is not isostructural with $BaGeTeO_6$ as was previously reported. Structural characterizations were carried out using a variety of tools, including Rietveld refinements of X-ray and neutron powder diffraction data, solid-state MAS–NMR, and Raman and infrared spectroscopy. With the exception of $M = Ti^{4+}$, the $MTeO_6^{2-}$ layers show a high degree of order between M^{4+} and Te^{6+} cations within the layers, but the stacking faults are generally present, which results in a significant decrease in the long-range ordering of the M^{4+} and Te^{6+} cations in the third dimension. The compound $K_{2-x}Na_xTiTeO_6$ was prepared by reacting Na_2TiTeO_6 and KNO_3 under hydrothermal conditions at 200°C in a Teflon-lined Parr bomb. This compound adopts a pyrochlore structure with cell edge 10.18 Å. NMR measurements indicate a disordered Ti/Te distribution. © 1999 Academic Press

INTRODUCTION

The $A_2M^{4+}\mathrm{Te}^{6+}\mathrm{O}_6$ family of compounds can be viewed as quaternary analogs of the $A\mathrm{SbO}_3$ family with a double substitution for antimony. Several different structure types are found among the ternary alkali antimonates, $A\mathrm{SbO}_3$. Staggered chains of edge-sharing SbO_6 octahedra are found in $LiSbO_3$ (1). The most common polymorph of $NaSbO_3$ adopts the ilmenite structure, containing sheets of edge-sharing SbO_6 octahedra (2). $KSbO_3$ also crystallizes in the ilmenite structure under typical synthesis conditions (3), but transforms to a cubic phase after prolonged heating (3) or under high pressure (4). The cubic $KSbO_3$ structure is built up of pairs of edge-sharing SbO_6 octahedra linked at the corners to form a three-dimensional network. $NaSbO_3$ can also be synthesized with the cubic $KSbO_3$ structure through ion exchange of the potassium compound (5). In addition, both $NaSbO_3$ and $KSbO_3$ have been reported with the pyrochlore structure (6, 7). The pyrochlore structure is the only structure type reported for $AgSbO_3$ (6, 8). The diversity of structures observed among the $A\mathrm{SbO}_3$ compounds strikingly demonstrates the way in which the size and polarizability of the A^{1+} cations can influence the structure and dimensionality of the SbO_3^{1-} network.

Most of the compounds synthesized in this work have structures that are derived from one of the layered $A_x\mathrm{SbO}_3$ compounds: $NaSbO_3$, α-$TlSbO_3$ (space group $P\bar{3}1c$, $PbSb_2O_6$, and β-$TlSbO_3$ (space group $P6_322$). In each case the parent antimonate structure can be constructed beginning from a hexagonal close packing of oxygens, with both Sb^{5+} and A^+ cations occupying octahedral holes in the oxygen lattice. In all four structures the A cations and the antimony ions are segregated into layers; the oxygen ions are always found to be shifted along the c axis toward the

---

[1] Current address: Department of Chemistry, Ohio State University, Newman and Wolfrom Laboratory, 100 W. 18th Avenue, Columbus, OH 43210-1185.

0022-4596/99 $30.00

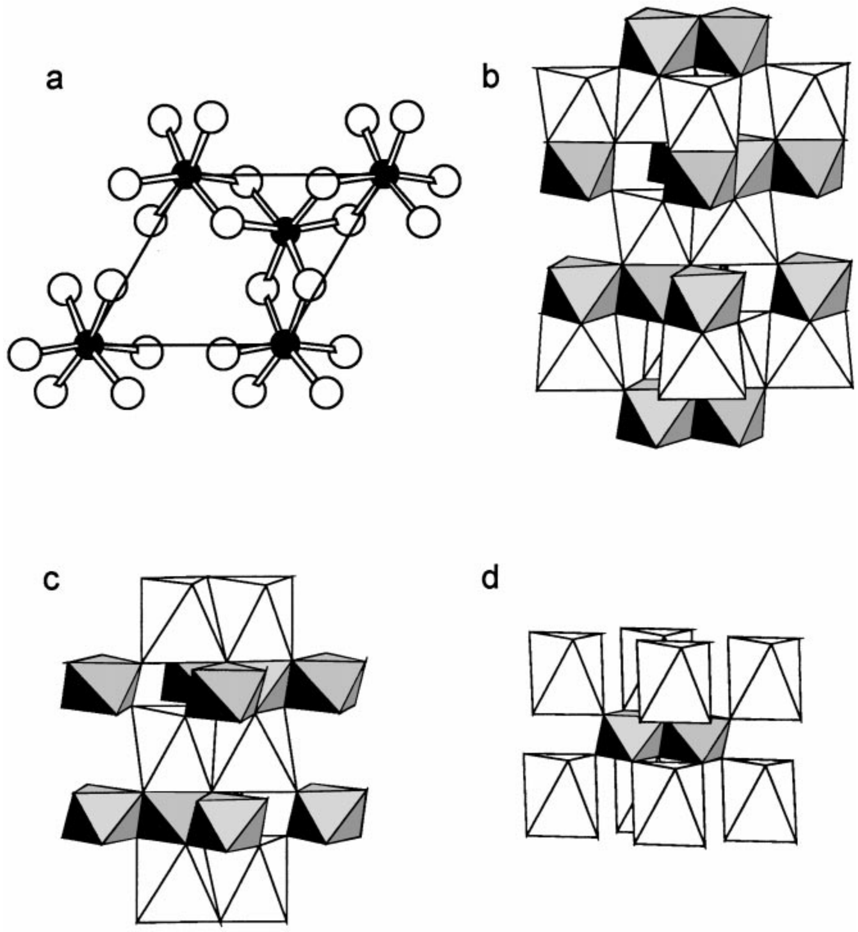

FIG. 1. Structural features of A_xSbO$_3$ compounds: (a) The SbO$_3^-$ layer with the antimony ions shown in black and the oxygen ions in white, (b) the three-layer NaSbO$_3$ (ilmenite) structure, (c) the two-layer α-TlSbO$_3$ ($P\bar{3}1c$) structure, and (d) the one-layer Pb$_{0.5}$SbO$_3$ structure. In each case the antimony octahedra are shaded, and the A cation octahedra are in white.

smaller Sb^{5+} ions. Because the Sb–O bonds are much stronger than the A–O bonds, the antimony oxide layers can be thought of as the basic structural building block of these compounds. This structural unit, shown in Fig. 1a, is essentially the same in all four structures. The antimony ions occupy two-thirds of the octahedral holes in the layer, while the remainder of the octahedral holes are vacant. Each SbO$_6$ octahedron shares edges with three other SbO$_6$ octahedra to form an infinite sheet. Both antimony ions and the vacancies are located on threefold axes, at $(0, 0, z)$, $(\frac{1}{3}, \frac{2}{3}, z)$, and $(\frac{2}{3}, \frac{1}{3}, z)$. The repulsion between the Sb^{5+} cations across the shared octahedral edges causes the layers to be stretched in the *ab* plane and flattened in the *c* direction. The SbO$_6$ octahedra are thus compressed in the direction parallel to the threefold axis. The smallest O–Sb–O angles in NaSbO$_3$ (2), TlSbO$_3$ (9), and PbSb$_2$O$_6$ (10) are 79.7°, 78.9°, and 79.5°, respectively. This distortion also helps to accommodate the larger A^{1+} cations, which sesparate SbO$_3^{1-}$ layers.

The NaSbO$_3$, α-TlSbO$_3$ ($P\bar{3}1c$), β-TlSbO$_3$ ($P6_322$), and PbSb$_2$O$_6$ structures differ from each other in the stacking of the antimony oxide layers and the arrangement of the A cations between the layers. In the PbSb$_2$O$_6$ structure the number of A cations and octahedral vacancies in the SbO$_3^{-1}$ layer are equal. Consequently, the A cations sit directly above and below the vacant octahedral sites in the neighboring SbO$_3^{-1}$ layers. This results in an AO$_6$ octahedron that shares six edges but no faces with neighboring SbO$_6$ octahedra. Viewing this structure down the *c* axis, one observes columns of A^{2+} cations confined to one threefold axis, and columns of Sb^{5+} cations on the remaining two threefold axes. Thus, each SbO$_3$ layer can be related to its neighboring layers by a translation of one layer in the *z* direction. This simple stacking arrangement leads to a unit cell containing a single SbO$_3$ layer. The polyhedral depiction of this structure is shown in Fig. 1b.

There has been some controversy surrounding the correct crystallographic description of compounds in the ASb$_2$O$_6$

family. Magnéli first made several ASb_2O_6 and AAs_2O_6 compounds and reported the structures in space group $P312$, using intensities estimated from powder X-ray diffraction photographs (11). This structural description gives two crystallographically nonequivalent antimony (arsenic) sites. However, the structure can also be described using space group $P\bar{3}1m$ with crystallographically equivalent antimony sites and very little change in the atomic coordinates. In an effort to resolve this discrepancy, two fairly recent structure determinations have been conducted. The first study involved determination of the $CaAs_2O_6$ structure from powder X-ray diffraction data (12). In that study, refinements using $P\bar{3}1m$ resulted in unrealistic oxygen positions, leading to the conclusion that $P312$ was indeed the correct space group (10). A later study of $PbSb_2O_6$ with powder neutron diffraction data reached the opposite conclusion, that $P\bar{3}1m$ was the correct space group (22). Any structure described in $P\bar{3}1m$ can be equally be described in $P312$ because the latter is the acentric subgroup of the former. It is possible that both acentric and centric versions of this structure actually exist, in which case some members of this family are potentially ferroelectric. The structures of $BaSb_2O_6$, $SrSb_2O_6$, and $CaSb_2O_6$ have most recently been reported to crystallize with $P\bar{3}1m$ symmetry (13).

$TlSbO_3$ exists as two polymorphs, α-$TlSbO_3$ belongs to space group $P\bar{3}1c$, while β-$TlSbO_3$ has $P6_322$ symmetry (9). The metal positions and unit-cell size are nearly identical in both structures, but they differ in the arrangement of oxygen ions. Both structures contain the same SbO_3 layers present in $PbSb_2O_6$, but there are now twice as many A cations as there are octahedral vacancy sites. Therefore, some of the SbO_6 octahedra are forced to share faces AO_6 octahedra. In both polymorphs of $TlSbO_3$ this leads to two distinct SbO_6 octahedra present in equal concentrations. The SbO_6 octahedron centered at the origin does not share faces with Tl-centered polyhedra, while the remaining SbO_6 octahedra share two faces with TlO_6 polyhedra. Each thallium ion is then shifted along the c axis away from the shared face and toward the face adjoining an octahedral vacancy. The difference between the two polymorphs is that in α-$TlSbO_3$ ($P1c$) the oxygen atoms are arranged so that the thallium is in octahedral coordination, whereas in β-$TlSbO_3$ ($P6_322$) the oxygen atoms form a trigonal prism about thallium. Both polymorphs have a unit cell that contains two SbO_3 layers. A polyhedral representation of the $P\bar{3}1c$ structure is shown in Fig. 1c.

Although $NaSbO_3$ has several polymorphs, we will be concerned here only with the ilmenite polymorph. In this structure each layer can be related to the previous layer by a rhombohedral translation vector $(\frac{2}{3},\frac{1}{3},\frac{1}{3})$, as can the positions of the sodium ions. This leads to a structure where all of the antimony ions are crystallographically equivalent. Each SbO_6 octahedron shares one face with a neighboring NaO_6 octahedron. As in the α-$TlSbO_3$ structure, the A cation shifts away from antmony and toward an octahedral vacancy. This stacking sequence has symmetry elements consistent with space group $R\bar{3}$. Although the primitive cell contains only one formula unit, the triple hexagonal cell contains three SbO_3 layers. A polyhedral representation of the ilmenite structure is shown in Fig. 1b.

Several compounds in the $A_2M^{4+}Te^{6+}O_6$ family have been synthesized and structurally characterized. Li_2TiTeO_6 and Li_2SnTeO_6 crystallize in a structure that can be derived from the $LiSbO_3$ structure by superposition of Ti/Te and Sn/Te ordering, respectively (14), Li_2ZrTeO_6 and Li_2HfTeO_6 also have ordered M^{4+}/Te^{6+} distributions; however, their structures can be derived from the $LiNbO_3$ structure rather than the $LiSbO_3$ structure (15). Among possible $A_2M^{4+}TeO_6$ compounds where A is either sodium or potassium, there are only four compositions reported in the literature. Na_2ZrTeO_6 is reported to be a distorted perovskite (16). An ordered distribution of cations is implied, but no structural refinement is given. The pyrochlore structure with a disordered distribution of Ge^{4+} and Te^{6+} is reported for K_2GeTeO_6, Rb_2GeTeO_6, and Cs_2GeTeO_6 (17).

Considering the many possible combinations of A and M^{4+} cations, many more members of the $A_2M^{4+}TeO_6$ family might be expected. This paper describes the synthesis and characterization of such compounds. This allows for a more thorough understanding of the structure determining forces in these compounds. The occurrence of compounds with cation distributions ranging from fully ordered to disordered also provides a good opportunity to study order–disorder phenomena and the factors that dictate the ordering behavior of the M^{4+}/Te^{6+} cations. In order to understand the ordering behavior of these compounds better, the study also encompasses $AGeTe^{6+}O_6$ (A = Ca, Sr, Ba) compounds. Cation ordering and local structure are probed with IR, Raman, and MAS–NMR spectroscopies. These spectroscopic techniques are highly complimentary to structure solution via diffraction methods, particularly for compounds having two or more nuclei with similar X-ray and neutron scattering factors. In such cases, where elements cannot be distinguished by diffraction techniques (e.g., F^- and O^{2-} in oxyfluorides, Sn^{4+} and Te^{6+} in Na_2SnTeO_6 in this paper), NMR can act as a complementary, element-selective method for determining both local structure and long-range order.

EXPERIMENTAL

All compounds were synthesized from stoichiometric mixtures of the alkali carbonates (Li_2CO_3, Na_2CO_3), alkaline-earth carbonates or nitrates ($CaCO_3$, $Sr(NO_3)_2$, $BaCO_3$), and the appropriate metal dioxides (TeO_2, GeO_2, SnO_2, and TiO_2). All reactant mixtures were subjected to an initial heat treatment at 600°C for 12–16 h to ensure that all of the tellurium was oxidized to the hexavalent state. Then each sample was heated again to successively higher temperatures until a single phase product was obtained. Temperature intervals were typically 50°C, beginning at 700°C, and dwell times at each temperature were 12–36 h.

Synthesis of Na_2SnTeO_6 in the manner described above always resulted in the presesnce of Na_2TeO_4 and SnO_2 in addition to the desired phase. If the temperature was increased ($>850°C$) in an attempt to drive the reaction toward completion, reduction and possibly volatilization of Te^{6+} occurred. To circumvent this problem, SnO_2 and Na_2CO_3 were first reacted near 1000°C to form Na_2SnO_3. A stoichiometric mixture of TeO_2 and Na_2SnO_3 was then heated first to 600°C and then to 700°C. This resulted in formation of a single-phase product. The same approach has previously been used to synthesize Li_2SnTeO_6 successfully (14).

Synchrotron X-ray diffraction data were obtained using the powder diffraction beamline X7A, at the National Synchrotron Light Source at Brookhaven National Laboratory. A channel-cut Si 111 monochromator was used to obtain monochromatic radiation. The samples were loaded into 0.2-mm diameter capillaries, which were freely rotated during data collection in order to reduce and hopefully eliminate preferred orientation effects (18). The diffracted radiation was detected using a linear position sensitive detector, which has been described elsewhere (19). Absorption corrections were applied, based on the measured sample densities of the filled capillaries, using a simple linear absorption correction. Neutron powder diffraction patterns were collected using large samples (~ 10 g) contained in either vanadium or aluminum cans on the high-resolution powder diffraction beamline (HPD) at the ANSTO reactor in Lucas Heights, Australia (Na_2TiTeO_6 and Na_2SnTeO_6) (20), and beamline BT1 at the NIST reactor in Gaithersburg, Maryland (β-Na_2GeTeO_6). Rietveld refinements (21) were carried out with the GSAS software package (22).

^{125}Te MAS–NMR spectra were obtained with a CMX-200 spectrometer at an operating frequency for ^{125}Te of 63.2 MHz. Aqueous $Te(OH)_6$ at 0 ppm was used as an external reference. A Chemagnetics pencil probe equipped with a MAS stator and 5.0-mm rotors that are capable of reaching spinning speeds of 12 kHz was used. Approximately 500 mg of sample was required for each experiment. Typically, spectra were acquired with $\pi/2$ pulses of 3 μs, recycle delays of 60 s, with each MAS spectrum requiring approximately 300–600 acquisitions.

The $^{125}Te/^{23}Na$ REDOR experiments were performed on a CMX-360 spectrometer with a triple resonance (HXY) probe with $\pi/2$ pulses for both ^{125}Te and ^{23}Na of 4.0 μs, at operating frequencies for ^{125}Te and ^{23}Na of 113.78 and of 95.23 MHz, respectively. Experiments were performed with the following REDOR pulse sequence (23, 24)

$$^{125}\mathrm{Te}\colon \pi/2–\tau–\quad –\tau–(\quad –\tau–\quad –\tau–)_n\pi–\tau–\quad –\tau–(\quad –\tau–\quad –\tau–)_n–\mathrm{acquire}$$

$$^{23}\mathrm{Na}\colon \qquad –\tau–\pi–\tau–(\pi–\tau–\pi–\tau–)_n\quad –\tau–\pi–\tau–(\pi–\tau–\pi–\tau–)_n,$$

where the interval τ is given by half the rotor period (i.e., 1/2 v_r where v_r is the spinning speed). A string of $2n+1$ ^{23}Na π pulses is applied during the evolution and refocusing period of the ^{125}Te spin echo experiment. The ^{125}Te π pulse, applied after $n+1$ rotor periods, serves to refocus the ^{125}Te chemical shifts. One experiment is performed with the ^{23}Na pulses and the intensity of the ^{125}Te resonance is measured (I). The experiment is repeated, without the Na pulses (the control experiment), in order to take into account any loss of ^{125}Te intensity due to T_2 effects. The intensity measured in the control experiment (I_0), and in the REDOR experiment (I) are then measured as a function of n, the number of rotor periods of dephasing. A REDOR fraction ($1 - I/I_0$) is then calculated for each value of n. The REDOR fraction is then plotted as a function of dephasing time ($(n+1) \times 1/v_r$)). The ^{23}Na frequency was applied exactly on resonance to minimize resonance offset effects.

RESULTS

X-Ray and Neutron Diffraction

Structural refinements using the Rietveld method were conducted for all compounds synthesized. Tables 1–4 list the results of these refinements, while the metal–oxygen bond distances are contained in Table 5. Li_2GeTeO_6, Na_2TiTeO_6, and α-Na_2GeTeO_6 all have unit cells very similar to the ilmenite form of $NaSbO_3$. Consequently, they were first refined in space group $R\bar{3}$ beginning from the $NaSbO_3$ structure, where the antimony site is occupied by a statistical mixture of Te and either Ge or Ti. In each case this led to a stable refinement. Next, the inversion center was eliminated, lowering the space group symmetry to $R3$, thereby allowing ordering of Te and Ge/Ti to occur. When the symmetry was lowered, no improvement in fit was observed for α-Na_2GeTeO_6 and Na_2TiTeO_6. Whereas, for Li_2GeTeO_6 the value of R_{wp} dropped from 5.30% to 4.98% and the refined occupancies suggested a partial ordering of Te and Ge. Another consequence of eliminating the inversion center is that the Ge/Te cations are no longer coplanar. In Li_2GeTeO_6, the Te and Ge ions are displaced from each other, in the z direction by 0.20 Å. Since this buckling of layers is not allowed in the centrosymmetric ilmenite structure, this distortion appears to be driven by the differences in size and/or charge between Ge^{4+} and Te^{6+}. The structure of Li_2GeTeO_6 is shown in Fig. 2.

The diffraction pattern collected on the Na_2GeTeO_6 sample, that had been prepared at 700°C, contained several

TABLE 1
Results of Rietveld Refinements of Three-Layer $A_2M\text{TeO}_6$ Compounds

Compound	Li_2GeTeO_6	α-Na_2GeTeO_6[a]	Na_2TiTeO_6
Synthesis temperature (°C)	750°C	700°C	750°C
Radiation	Synchrotron	Synchrotron	Neutron
λ (Å)	0.50275	0.50275	1.4945
Space group	$R3$	$R\bar{3}$	$R\bar{3}$
R_{wp} (%)	4.98	4.92	8.55
$R(F^2)$ (%)	5.48	4.32	7.07
a (Å)	5.00795 (5)	5.10118(4)	5.2201(2)
c(Å)	14.3422(2)	15.9590(2)	15.8375(6)
Volume (Å^3)	311.506(6)	359.648(5)	373.74(3)
Volume/Z (Å^3)	103.835	119.983	124.58
a/c	1.048	0.959	0.989
2θ range	4–67°	4–45°	12–152°
Number of reflections	654	616	201
Number of variables	26	27	17

Atom	Site	x	y	z	B_{iso}	Occupation
Li_2GeTeO_6						
Li(1)	3a	0	0	0.132(5)	3.2(3)	1.0
Li(2)	3a	0	0	0.866(5)	3.2(3)	1.0
Ge(1)	3a	0	0	0.65969(4)	0.355(6)	0.816(8)
Te(1)	3a	0	0	0.65969(4)	0.355(6)	0.184(8)
Te(2)	3a	0	0	0.34031(4)	0.355(6)	0.816(8)
Ge(2)	3a	0	0	0.34031(4)	0.355(6)	0.184(8)
O(1)	9b	0.309(2)	− 0.024(2)	0.2593(8)	0.36(5)	1.0
O(2)	9b	0.725(2)	0.040(2)	0.7400(9)	0.36(5)	1.0
α-Na_2GeTeO_6						
Na	6c	0	0	0.1413(1)	1.20(4)	1.0
Ge	6c	0	0	0.3373(9)	0.22(1)	0.5
Te	6c	0	0	0.3373(9)	0.22(1)	0.5
O	12i	0.2797(4)	− 0.0491(4)	0.2651(1)	0.37(5)	1.0
Na_2TiTeO_6						
Na	6c	0	0	0.1409(2)	0.89(6)	1.0
Ti	6c	0	0	0.3378(6)	− 0.2(1)	0.5
Te	6c	0	0	0.3378(6)	− 0.2(1)	0.5
O	18f	0.2736(3)	− 0.0518(3)	0.2640(1)	0.69(2)	1.0

[a] There was 4 wt% of β-Na_2GeTeO_6 present, which was refined as a second phase.

weak "impurity peaks." In an effort to eliminate this unknown second phase, the sample was heated to 750°C for 36 h. An X-ray diffraction pattern obtained after the 750°C anneal showed a single-phase pattern, but surprisingly it was not the same phase that had dominated the pattern prior to the heating cycle. The phase that appeared at 750°C corresponded to the "impurity peaks" in the 700°C sample. (A later two-phase refinement showed that the sample prepared at 700°C contained 96% of the ilmenite polymorph and 4% of the high temperature phase). The X-ray diffraction patterns of Na_2GeTeO_6 annealed at 700 and 750°C are shown in Fig. 3. Closer inspection revealed that the new unit cell was also trigonal with the same a axis and a c axis that was two-thirds the value of the former c axis. The extinction conditions indicated a P–c space group symmetry. The values of the cell edges suggested that the structure contained the same $GeTeO_6^{2-}$ layers as the ilmenite structure, but the unit cell now contained two layers instead of three. Of the five space groups that corresponded to the observed extinction conditions ($P31c$, $P\bar{3}1c$, $P6_3mc$, $P\bar{6}2c$, and $P6_3/mmc$), atomic positions consistent with a two-layer stacking were possible only in $P31c$ and $P\bar{3}1c$. On the basis of electrostatic considerations a starting model was chosen where the NaO_6 octahedra share edges only with GeO_6. This led to a stable refinement with low residuals and good agreement with the experimental data. Allowing the Ge and Te sites to mix resulted in a marginally better fit to the synchrotron data, but no improvement to the neutron data.

TABLE 2
Results of Rietveld Refinements of Two-Layer $A_2M\mathrm{TeO}_6$ Compounds

Compound	Na_2SnTeO_6	β-Na_2GeTeO_6
Synthesis temperature (°C)	700°C	750°C
Radiation	Neutron	Neutron
λ (Å)	1.4945	1.5401
Space group	$P\bar{3}1c$	$P\bar{3}1c$
R_{wp} (%)	7.53	5.74
$R(F^2)$ (%)	6.92	4.17
a (Å)	5.3416(1)	5.09580(5)
c (Å)	10.6991(3)	10.6325(1)
Volume (Å^3)	264.37(1)	239.106(6)
Volume/Z (Å^3)	132.19	119.55
a/c	0.999	0.959
2θ range	10–154°	10–156°
Number of reflections	217	183
Number of variables	16	17

Atom	Site	x	y	z	B_{iso}	Occupation
Na_2SnTeO_6						
Na	$4f$	$\frac{2}{3}$	$\frac{1}{3}$	0.9534(2)	0.63(8)	0.92(1)
Te	$2d$	$\frac{2}{3}$	$\frac{1}{3}$	$\frac{1}{4}$	0.47(5)	1.0
Sn	$2a$	0	0	$\frac{1}{4}$	0.51(4)	1.0
O	$12i$	0.0589(2)	0.7069(3)	0.6455(1)	0.66(2)	1.0
β-Na_2GeTeO_6						
Na	$4f$	$\frac{2}{3}$	$\frac{1}{3}$	0.9617(2)	1.08(3)	1.0
Ge	$2d$	$\frac{2}{3}$	$\frac{1}{3}$	$\frac{1}{4}$	0.36(2)	1.0
Te	$2a$	0	0	$\frac{1}{4}$	0.42(3)	1.0
O	$12i$	0.0536(2)	0.7162(2)	0.64862(6)	0.59(1)	1.0

Therefore, complete Ge/Te ordering was assumed. Removing the inversion center and lowering the symmetry $P31c$ did not improve the fit.

Na_2SnTeO_6 showed extinction conditions and cell edges suggesting that it is isostructural with the ordered variant of Na_2GeTeO_6. Refinements indicated that although the structures are similar, they differ in one important aspect. In Na_2SnTeO_6, the TeO_6 octahedra share faces with NaO_6 octahedra, rather than the SnO_6 octahedra. This is confirmed not from the occupancies of the Sn^{4+} and Te^{6+}, which cannot easily be distinguished using either X-ray or neutron diffraction, but from the positions of the oxygen ions, which are displaced away from the bigger tin ion toward tellurium. The structure of Na_2SnTeO_6 is shown in Fig. 4. That Na shares a face with Te, instead of Sn, might seem surprising, because it is in contradiction to what would be expected from a simple consideration of the formal charges in the compound. This observation is, however, supported by the $^{125}Te/^{23}Na$ REDOR experiments reported later in the NMR section and will be further examined in the Discussion section.

Refinements using both X-ray and neutron diffraction data indicated that the sodium sites in Na_2SnTeO_6 were only partially ($\sim$ 90%) occupied. Because the sample was heated to over 1000°C before adding the TeO_2, it is certainly possible that some sodium volatilized during the synthesis. The most probable charge-compensating mechanism is partial replacement of Sn^{4+} with Te^{6+}, to yield a stoichiometry of $Na_{1.8}Sn_{0.9}Te_{1.1}O_6$. It is difficult to confirm this from the diffraction data because Sn^{4+} and Te^{6+} are isoelectronic and, therefore, are essentially identical to X-rays. The situation improves only slightly with neutrons, because the scattering lengths ($Sn = 0.623$, $Te = 0.580$) are quite similar. Rietveld refinements using the neutron data gave essentially the same residuals based on a

TABLE 3
Results of Rietveld Refinements of One-Layer $AM\mathrm{TeO}_6$ Compounds

Compound	$SrGeTeO_6$	$BaGeTeO_6$[a]
Synthesis Temperature (°C)	900°	860°C
Radiation	Synchrotron	Synchrotron
λ (Å)	0.57775	0.57775
Space group	$P312$	$P312$
R_{wp} (%)	5.36	9.03
$R(F^2)$ (%)	13.36	9.87
a (Å)	5.06566(3)	5.09496(3)
c (Å)	5.40394(5)	11.57963(9)
Volume (Å^3)	120.092(2)	260.319(3)
Volume/Z (Å^3)	12.092	130.160
a/c	0.937	0.880
2θ range	3–62°	4–62°
Number of reflections	282	598[b]
Number of variables	14	22

Atom	Site	x	y	z	B_{iso}	Occupation
$SrGeTeO_6$						
Sr	$1a$	0	0	0	0.96(2)	1.0
Ge	$1f$	$\frac{2}{3}$	$\frac{1}{3}$	$\frac{1}{2}$	0.63(1)	1.0
Te	$1d$	$\frac{1}{3}$	$\frac{2}{3}$	$\frac{1}{2}$	0.63(1)	1.0
O	$6l$	0.380(1)	0.005(1)	0.3111(6)	1.08(8)	1.0
$BaGeTeO_6$						
Ba	$2g$	0	0	0.2478(4)	0.82(2)	1.0
Ge(1)	$1c$	$\frac{1}{3}$	$\frac{2}{3}$	0	0.47(1)	0.90(1)
Te(1)	$1c$	$\frac{1}{3}$	$\frac{2}{3}$	0	0.47(1)	0.10(1)
Te(2)	$1e$	$\frac{2}{3}$	$\frac{1}{3}$	0	0.47(1)	0.90(1)
Ge(2)	$1e$	$\frac{2}{3}$	$\frac{1}{3}$	0	0.47(1)	0.10(1)
Ge(3)	$1d$	$\frac{1}{3}$	$\frac{2}{3}$	0.5	0.47(1)	0.90(1)
Te(3)	$1d$	$\frac{1}{3}$	$\frac{2}{3}$	0.5	0.47(1)	0.10(1)
Te(4)	$1e$	$\frac{2}{3}$	$\frac{1}{3}$	0.5	0.47(1)	0.90(1)
Ge(4)	$1e$	$\frac{2}{3}$	$\frac{1}{3}$	0.5	0.47(1)	0.10(1)
O(1)[c]	$6l$	0.369(2)	− 0.003(2)	0.0899(8)	0.49(8)	1.0
O(2)[c]	$6l$	0.406(2)	0.002(2)	0.4039(8)	0.49(8)	1.0

[a] There was 3 wt% of $BaGe_4O_9$ present, which was refined as a second phase.

[b] In addition, there were 1239 reflections associated with $BaGe_4O_9$.

[c] A soft constraint was placed on the Ge–O distance (1.90 Å) and the Te–O distance (1.92 Å).

TABLE 4
Summary of the Refinement Results for AGeTeO$_6$ Compounds, Using the Various Structural Models Discussed in the Text

Model	Compound	$SrGeTeO_6$	$BaGeTeO_6$[a]
1	(R_{wp})	5.70%	—
	B_{iso} (oxygen)	0.804(8)	
	S*	0%	
2	(R_{wp})	—	9.37%
	B_{iso} (oxygen)		0.25(8)
	S*		0%
3	(R_{wp})	—	11.17%
	B_{iso} (oxygen)		1.6(1)
	S*		36(2)%
4	(R_{wp})	—	9.36%
	B_{iso} (oxygen)		0.69(7)
	S*		28(2)%
5	(R_{wp})	**5.33%**	—
	B_{iso} (oxygen)	**1.08(8)**	
	S*	**100%**	
6	(R_{wp})	6.61%	**9.03%**
	B_{iso} (oxygen)	3.6(2)	**0.49(8)**
	S*	86(2)%	**80(2)%**

[a] The long-range order parameter, $S = 2M - 1$, where M is the occupancy of Te on the Te-rich site(s) and the occupancy of Ge on the Ge-rich site.

$Na_{1.8}Sn_{1-x}Te_{1+x}O_6$ stoichiometry for $x = 0.1$ or 0. Refinements with the noncentrosymmetric space group $P31c$, which allows the layers to buckle, led to only a very slight improvement of the fit (R_{wp} decreased from 7.20 to 7.11% in the neutron data). Even this modest improvement was not possible without constraining the refinement. Therefore, the noncentrosymmetric $P31c$ model was rejected. In view of the ambiguous diffraction results. Te^{6+} substitution was studied by ^{125}Te NMR, as described in the NMR section.

Table 3 contains the refinement results for $SrGeTeO_6$ and $BaGeTeO_6$. Both compounds were previously synthesized by Robert and Tarte (25). They concluded, based on examination of the X-ray diffraction, infrared, and Raman spectra, that the most likely space group for both compounds was $P6_322$. This is consistent with the structural model originally proposed by Frydrych for the compounds $APbIO_6$ and $ASnIO_6$ (26, 27), and later confirmed for the A = Rb analog (28). This structure contains two layers in the unit cell, giving rise to a c axis that contains two SbO_3 (1) layers. The A cation is in trigonal prismatic coordination, and the smaller octahedral cations alternate in columns running parallel to the c axis (M–I–M–I–M–I–$\cdots$). An alternative model proposed by Kasper for the rare-earth compounds $LnCrTeO_6$ has a doubled c axis and the same cation ordering arrangement, but maintains the octahedral coordination of the A cation (29). A third possibility is a simple intralayer ordering of cations within the $PbSb_2O_6$ structure, which maintains a unit cell containing only one formula unit but lowers the symmetry from $P\bar{3}1m$ to $P312$. This structure has been found for $KGeTeO_6$ (30) and $RbGeIO_6$ (30).

For a variety of $AMM'O_6$ ($M = Te^{6+}, I^{7+}$) structures, a common feature is the $MM'O_6^{n-}$ layer shown in Fig. 1. Several permutations on the basic $PbSb_2O_6$ structure can be realized by altering the cation ordering and the A cation coordination. The structural possibilities for AGeTeO$_6$ compounds are as follows:

1. The Ge and Te cations are statistically distributed, and the A cation is in octahedral coordination. This results in the $PbSb_2O_6$ structure, space group $P\bar{3}1m$.
2. The Ge and Te cations are statistically distributed, and the A cation is in trigonal primatic coordination. This structure is consistent with space group $P\bar{3}1m$ with a doubled c axis.
3. The intralayer ordering is such that Ge and Te cations have only unlike near neighbors within each layer, and the opposite neighbors in the layers directly above and below, forming Ge–Te–Ge–Te–$\cdots$ columns parallel to the axis. The A cation is in octahedral coordination. This structure corresponds to Kasper's model and belongs to space group $P\bar{3}1c$ with a doubled c axis.
4. The same cation arrangement as model 3 with trigonal prismatic coordination of the A cation. This structure corresponds to Frydrych's model and belongs to space group $P6_322$ with a doubled c axis.

TABLE 5
Bond Distances in A_2MTeO$_6$ and AMTeO$_6$ Compounds

Compound	A–O distances (Å)	M–O distances (Å)[a]	Te–O distances (Å)
Na_2SnTeO_6	3 × 2.304(2)	6 × 2.072(1)	6 × 1.939(1)
	3 × 2.595(3)		
β-Na_2GeTeO_6	3 × 2.285(1)	6 × 1.9022(8)	6 × 1.9293(8)
	3 × 2.531(2)		
Na_2TiTeO_6	3 × 2.326(2)	3 × 1.943(5)	3 × 1.943(5)
	3 × 2.509(3)	3 × 1.966(6)	3 × 1.966(6)
α-Na_2GeTeO_6	3 × 2.283(2)	3 × 1.904(6)	3 × 1.904(6)
	3 × 2.522(2)	3 × 1.946(7)	3 × 1.946(7)
Li_2GeTeO_6	Li(1)		
	3 × 2.08(3)	3 × 1.88(1)	3 × 1.89(1)
	3 × 2.37(4)	3 × 1.90(1)	3 × 1.97(1)
	Li(2)		
	3 × 2.00(2)		
	3 × 2.39(4)		
$SrGeTeO_6$	6 × 2.544(4)	6 × 1.872(6)	6 × 1.907(5)
$BaGeTeO_6$		Ge(1)	Te(2)
	3 × 2.627(9)	6 × 1.91(1)	6 × 1.93(9)
	3 × 2.748(9)	Ge(3)	Te(4)
		6 × 1.90(1)	6 × 1.91(1)

[a] The M–O and Te–O distances refer to the Ge-rich and Te-rich sites, respectively, in α-Na_2GeTeO_6, Li_2GeTeO_6, and $BaGeTeO_6$. In Na_2TiTeO_6 there is a statistical distribution of Ti and Te, therefore, the M–O and Te–O distances are equal.

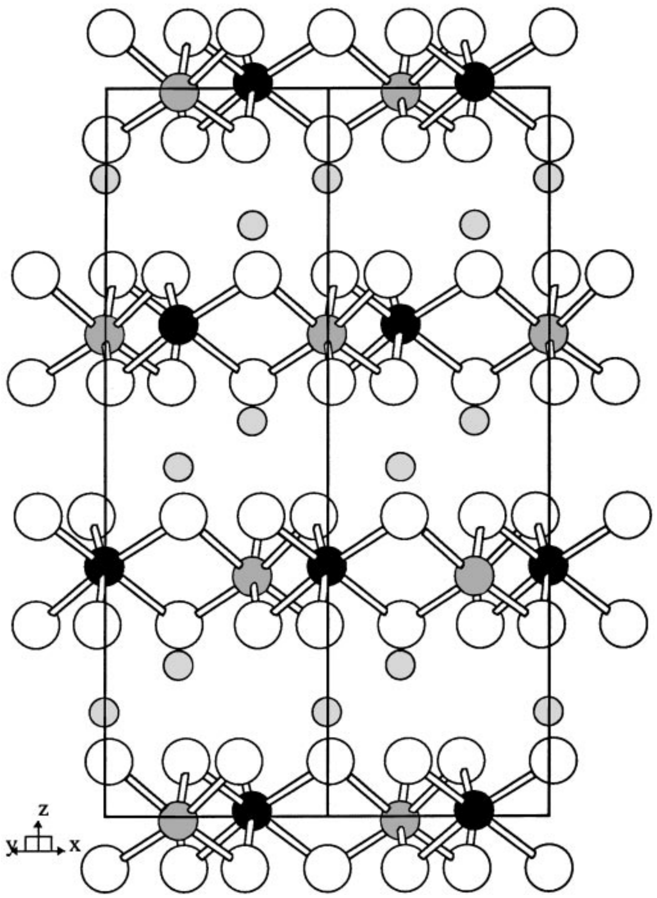

FIG. 2. The structure of Li_2GeTeO_6. The small shaded circles represent lithium ions, the open circles represent oxygen, the larger shaded circles represent the germanium rich octahedral site, and the black circles represent the tellurium rich site.

5. The intralayer ordering is such that Ge and Te cation have only unlike neighbors within each layer, and the same neighbors in the layers directly above and below, forming Ge–Ge–Ge–Ge–⋯ and Te–Te–Te–Te–⋯ columns parallel to the *c* axis. The *A* cation is in octahedral coordination. This structure can be generated in space group *P*312 with the $PbSb_2O_6$ cell.
6. The same cation arrangement as model 5 with trigonal prismatic coordination of the *A* cation. This structure can also be generated in space group *P*312, but the oxygen distribution necessitates a doubling of the *c* axis.

Proper indexing of the observed diffraction pattern can eliminate certain possibilities, because the size of the unit cell changes from one model to the next. A doubled *c* axis was necessary to index the reflections present in the X-ray diffraction pattern of $BaGeTeO_6$, eliminating models 1 and 5 from consideration. In contrast, $SrGeTeO_6$ could be indexed using a simple ($Z = 1$) unit cell, with no systematic absences. The absence of a doubled *c* axis strongly suggests that either model 1 or 5 correctly describes the structure of $SrGeTeO_6$.

The next step was to perform Rietveld refinements beginning from the various starting models listed above. The results are listed in Table 4. From the residuals and the value of the oxygen displacement parameters, it was possible to differentiate between models with the *A* cation in trigonal prismatic coordination and those with the *A* cation in octahedral coordination. Based on these refinements, the *A*-site coordination was found to be octahedral in $SrGeTeO_6$ and trigonal prismatic in $BaGeTeO_6$. The refinement results were less conclusive regarding the ordering of cations in the *c* direction. $SrGeTeO_6$ shows a high degree of ordering/coherence in the layer stacking, adopting a structure with columns of like cations (Ge–Ge–⋯ and Te–Te–⋯) running parallel to the *c* axis. The refinement results presented in Table 3 assume complete order in the layer stacking. A marginally better fit ($R_{wp} = 5.29\%$) could be obtained if Ge and Te were allowed to mix, yielding occupancies of 0.95 and 0.05 for the majority and minority ions on each site (S = 90%). Unfortunately, this also resulted in less realistic Ge–O and Te–O distances, implying a correlation between the cation order parameter and the oxygen positions. Thus, a model with complete Ge/Te order was employed, but the experimental data do not conclusively rule out the possibility that a limited number of stacking

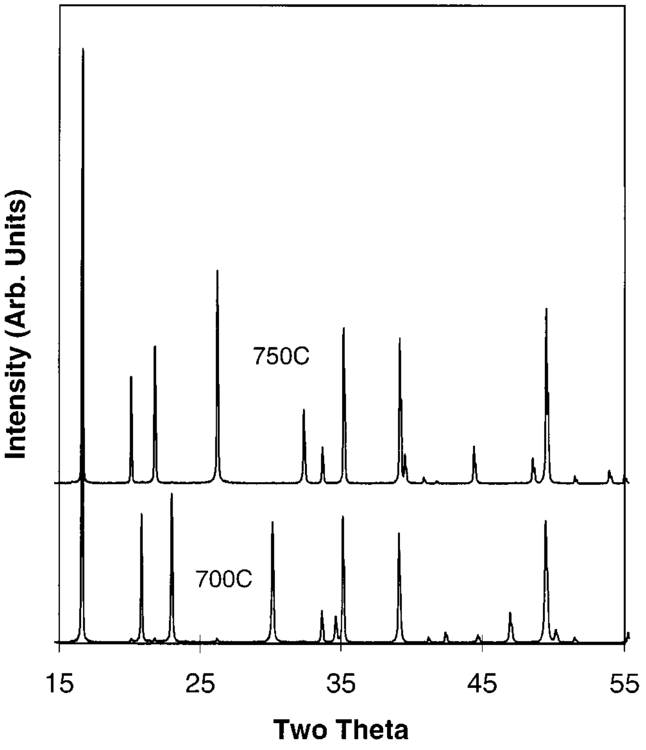

FIG. 3. The X-ray diffraction spectra of Na_2GeTeO_6 after annealing at 700°C (lower pattern) and 750°C (upper pattern).

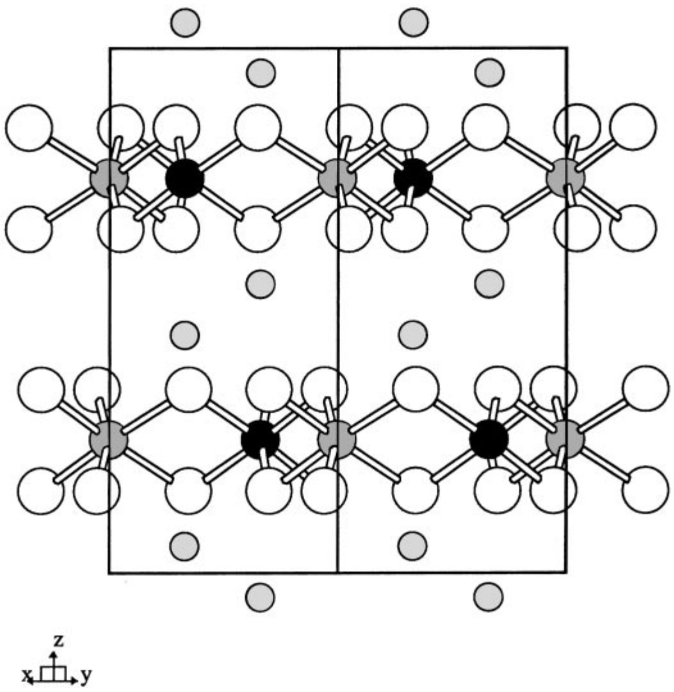

FIG. 4. The structure of Na_2SnTeO_6. The small shaded circles represent sodium, the open circles represent oxygen, the larger shaded circles represent tin, and the black circles represent tellurium.

faults are present in $SrGeTeO_6$. Refinements indicate that the predominant stacking sequence in $BaGeTeO_6$ is the same as that found in $SrGeTeO_6$. However, in this compound stacking faults are clearly present.

$CaGeTeO_6$ was also prepared and structurally analyzed using laboratory powder X-ray diffraction. No doubling of the *c* axis was detected, implying $CaGeTeO_6$ is isostructural with $SrGeTeO_6$. Rietveld refinements produced unrealistic Ge–O and Te–O distances; thus, further study is necessary to unambiguously characterize the structure of this compound.

Attempts to directly prepare K_2GeTeO_6, K_2GeTeO_6, and K_2SnTeO_6 by conventional methods were unsuccessful. attempts to prepare such phases from the analogous Na_2MTeO_6 phases by ion exchange in a boiling solution of KNO_3 or in molten KBr also failed. Treating Na_2TiTeO_6 with aqueous KNO_3 at 200°C in a Teflon-lined Parr bomb led to a product with the pyrochlore structure with a cubic cell edge of 10.18 Å. Initial characterization of this compound indicates partial substitution of potassium for sodium; however, further study is necessary to characterize the structure and composition of this new pyrochlore definitively.

Vibrational Spectroscopy

The vibrational spectra of several complex oxides containing hexavalent tellurium have been recorded and interpreted with some degree of success, primarily by Tarte and coworkers (14, 15, 25, 31, 32). Due to the ambiguity associated with characterizing the disorder in these systems from diffraction data, complementary structural analysis tools were needed. These factors prompted a study of the vibrational spectra of the quaternary tellurium oxides synthesized in this work.

Figures 5 and 6 show the infrared and Raman spectra, respectively, for several of the A_xGeTeO_6 compounds prepared. Figures 7 and 8 show the infrared and Raman spectra of the Na_2MTeO_6 (M = Ti, Ge, Sn) compounds. Considering first the germanium containing compounds, the most striking feature evident in Fig. 5 and 6 is the great similarity between the various compounds in the infrared and especially in the Raman spectra. The band widths are comparable across the entire series of compounds. The band positions and intensities are also quite similar from one compound to the next, but small variations and shifts are present. Comparing the structures of these compounds, the common feature is the $GeTeO_6^{2-}$ layers, while the space group, identity and concentration of the A cation, and stacking arrangment of the layers all vary significantly from one compound to the next. Thus, two points can be immediately inferred from the vibrational spectra. First, intralayer vibrations dominate the infrared and Raman spectra of these compounds. Second, the layer structure and degree of cation order within each layer appear to be quite similar

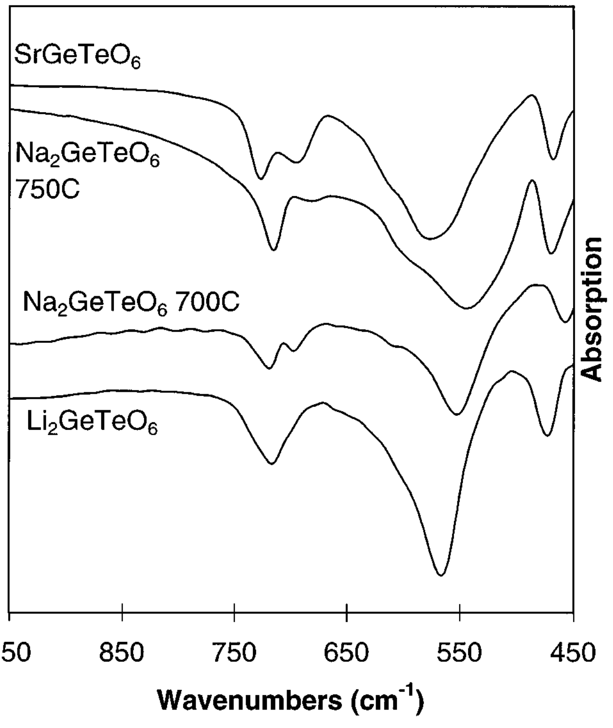

FIG. 5. The infrared spectra of A_xGeTeO_6 compounds.

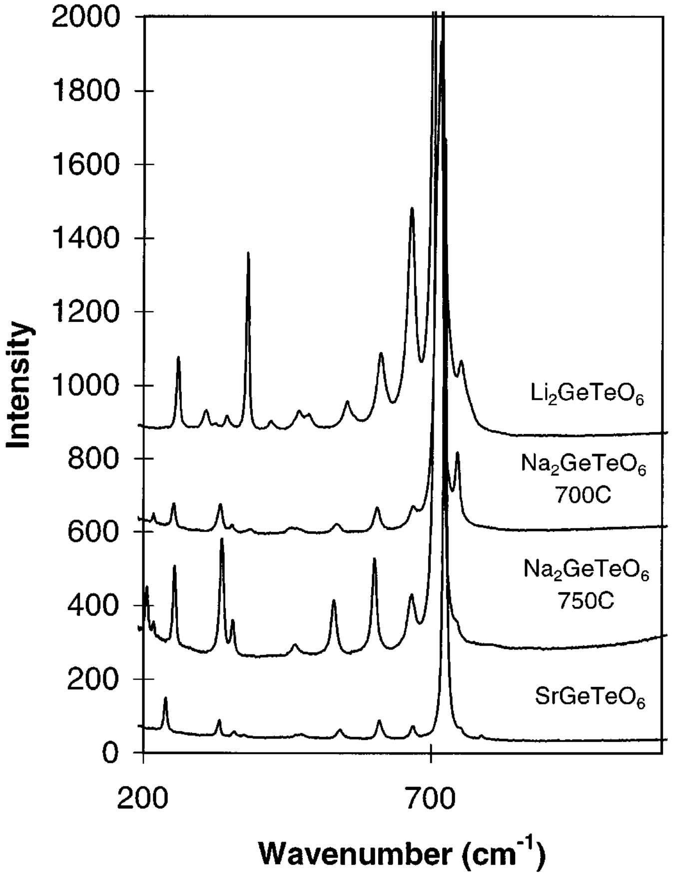

FIG. 6. The Raman spectra of $A_x\mathrm{GeTeO}_6$ compounds.

throughout the entire series of compounds. The sharp bands present in these spectra are indicative of an ordered distribution of Ge and Te (9). Extending this analysis to $\mathrm{Na_2TiTeO_6}$ and $\mathrm{Na_2SnTeO_6}$, the broad Raman lines associated with the former compound imply disorder on a local scale (intralayer), while the sharp Raman lines observed for $\mathrm{Na_2SnTeO_6}$ suggest a high degree of local order. Both conclusions are in agreement with the diffraction results.

Based on the symmetry of the space group and the symmetry of the occupied sites in the lattice the number of infrared active, Raman active, and coincident modes can be predicted (33). Table 6 lists the predicted number of each type of mode for several real and hypothetical structures. Table 7 lists the number of each type of mode observed in the compounds under study. Because the infrared spectra were only collected to 400 cm^{-1}, the total number of infrared active modes and coincident modes may be higher than listed in Table 7. All of the compounds analyzed were found to have modes coincident to both the Raman and infrared spectra. This is direct evidence for the lack of an inversion center in the lattice. Furthermore, the number of Raman modes observed for each compound varied from one compound to the next and was in several cases greater than expected for isolated $M\mathrm{TeO}_6^{2-}$ layers. Thus, interactions between the alkali/alkaline-earth cations and the $M\mathrm{TeO}_6^{2-}$ layers do appear to have some influence on the vibrational spectra. Another feature worth noting is the fact that the number of modes observed in the Raman and IR spectra increases as the disorder in the cation distribution increases. This is in direct contradiction to what is expected based on modeling using the crystallographic unit cell where in a disordered compound M^{4+} and Te^{6+} share a crystallographically equivalent site. The explanation for this contradiction is that diffraction is sensitive to long-range order, whereas the vibrational spectra are sensitive to local symmetry and short-range order. By increasing the long range order, the number of local coordination configurations decreases. Consequently, the number of vibrational modes observed reaches a minimum when the long range order parameter is 100%.

The observation of coincident bands in the infrared and Raman spectra for all compounds studied, indicating a noncentrosymmetric space group, is in contradiction with the Rietveld refinement results for $\mathrm{Na_2SnTeO_6}$ and β-$\mathrm{Na_2GeTeO_6}$ (space group $P\bar{3}1c$), as well as $\mathrm{Na_2TiTeO_6}$ and α-$\mathrm{Na_2GeTeO_6}$ (space group $R\bar{3}$). The contradiction is easily reconciled for the $R\bar{3}$ compounds by noting that short range Ge/Te and Ti/Te ordering will destroy the inversion center.

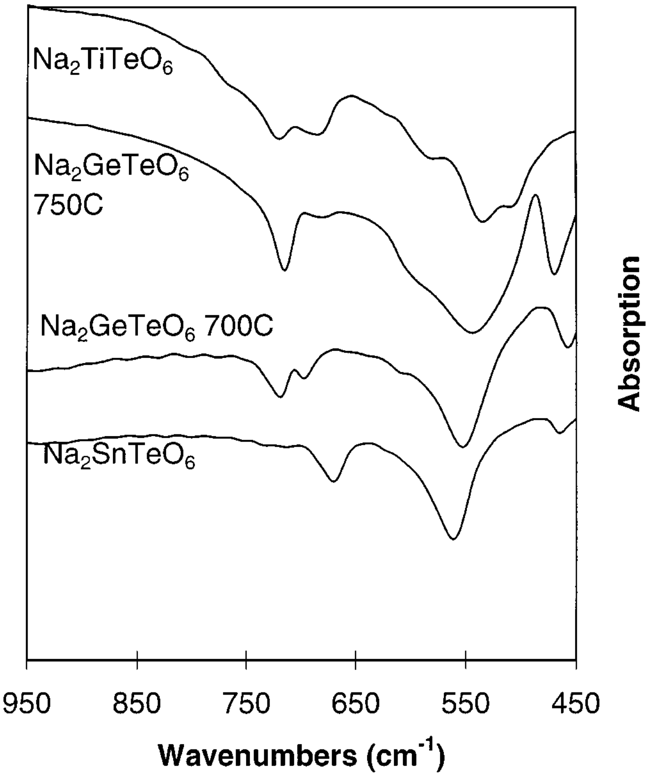

FIG. 7. The infrared spectra of $\mathrm{Na_2}M\mathrm{TeO_6}$ compounds.

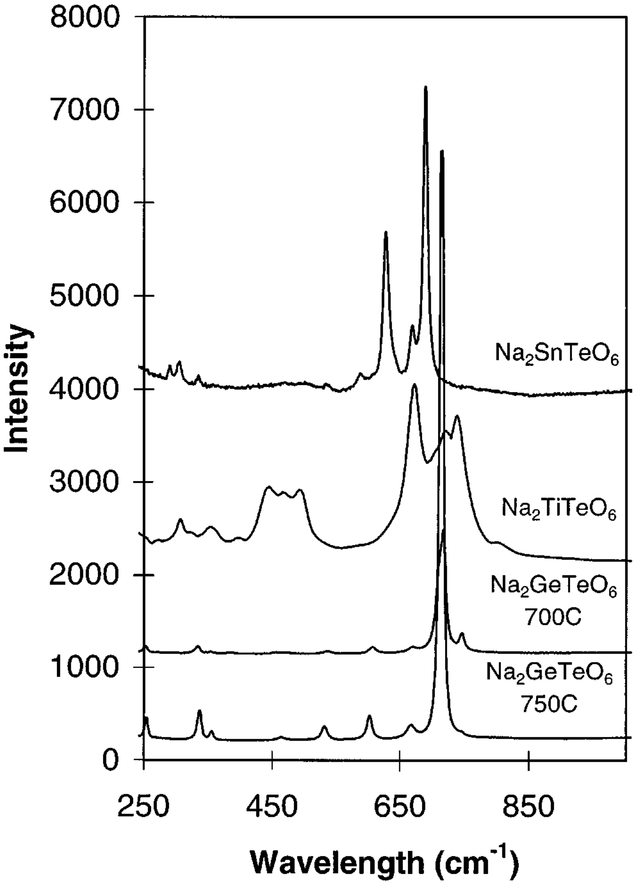

FIG. 8. The Raman spectra of Na_2MTeO_6 compounds.

TABLE 6
Number of Vibrational Modes Predicted by Factor Group Analysis for Several Possible Structure Types Built Up from Trigonal $MTeO_6^{2-}$ Layers

			Number of active modes		
Layer stacking	Cation distribution	Space group	Infrared	Raman	Coincident
3-Layer "$NaSbO_3$"	Simple	$R\bar{3}$	8	10	0
	Ordered	$R3$	18	18	18
2-Layer "$TlSbO_3$"	Ordered	$P\bar{3}1c$	23	5	0
	Ordered	$P31c$	28	28	28
1-Layer "$PbSb_2O_6$"	Simple	$P\bar{3}1m$	7	6	0
	Ordered	$P312$	13	11	8
Isolated SbO_3^- layers	Simple	$P\bar{3}1m$	5	6	0
Isolated $MTeO_6^{2-}$ layers	Ordered	$P312$	11	10	7

Note. A simple cation distribution refers to a structure with a single ion (antimony) on the small octahedral sites, whereas an ordered disstributions refers to that expected for a perfectly ordered distribution of M^{4+}/Te^{6+} on the small octahedral sites.

Thus, on the short length scales probed by the IR and Raman methods the structure is noncentrosymmetric, while the average structure seen by diffraction is centrosymmetric. The discrepancy is more difficult to understand in the ordered $P\bar{3}1c$ compounds, where the local and average structures should be the same. In order try and reconcile these results, further refinements were carried out on Na_2GeTeO_6 and Na_2SnTeO_6, using the noncentrosymmetric space group $P31c$. In neither case could a better fit to the observed data be obtained. Furthermore, it is uncertain what structural feature could be responsible for destroying the inversion center. The most likely possibility would seem to be a buckling of the layers, which was observed in the ilmenites Li_2GeTeO_6 and Na_2GeTeO_6. However, refinements did not show any evidence that this actually occurs. Thus, there appears to be a contradiction between the vibrational spectra and the X-ray diffraction results for these two compounds. However, since the inversion center relates neighboring layers, the presence of some disorder in the layer stacking will destroy the strict centrosymmetry of the lattice. This may be sufficient to allow violation of the selection rule, which prohibits coincident modes in the infrared and Raman spectra. Another possibility is that the layers are actually buckled, but the layers do not buckle in a cooperative manner so that this distortion cannot be detected in the Rietveld refinements. Accidental coincidence is another possibility.

MAS-NMR Spectroscopy

Six samples were studied by ^{125}Te MAS-NMR: Na_2SnTeO_6, β-Na_2GeTeO_6, α-Na_2GeTeO_6, Li_2GeTeO_6, Na_2TiTeO_6, and $K_{2-x}Na_xTiTeO_6$. Samples were spun at 9 kHz to collect high-resolution spectra. Spectra were also acquired at lower MAS speeds and without MAS in order to study the tellurium local environment. CSA parameters were extracted by using the simulation program HBA

TABLE 7
Number of Vibrational Modes Observed for Several A_xMTeO_6 Compounds

		Number of active modes		
Compound	Layer stacking	Infrared	Raman	Coincident
Li_2GeTeO_6	3 layer	3	12	2
α-Na_2GeTeO_6	3 layer	5	11	2
Na_2TiTeO_6	3 layer	6	14	1
β-Na_2GeTeO_6	2 layer	4	10	2
Na_2SnTeO_6	2 layer	3	8	1
$SrGeTeO_6$	1 layer	5	12	2

Note. Raman spectra were collected down to 200 cm^{-1} and infrared spectra to 400 cm^{-1}. The layer stacking assignment is made based on the unit cell determined from X-ray diffraction.

TABLE 8
The ^{125}Te NMR[a] Results of A_xMTeO$_6$ Compounds

Compound	Layer stacking	α_{iso}[b] (ppm)	η[c]	$\Delta\sigma$[d] (ppm)	FWHM[e] (ppm)	Long-range order parameter[f]
Na_2SnTeO_6	2 layer	102.0	0.2	101	1.4	100%
β-Na_2GeTeO_6	2 layer	32.5	0.0	185	1.1	100%
Li_2GeTeO_6	3 layer	50.4	0.0	122	1.4	63%
α-Na_2GeTeO_6	3 layer	41.7	0.0	183	3.2	0%
Na_2TiTeO_6	3 layer	16.6			45.6	0%
$K_{2-x}Na_xTiTeO_6$	Pyrochlore	-62.1			53.8	0%

[a] All the NMR spectra were taken with a field strength of 4.7 T, except α-Na_2GeTeO_6, which was taken with a field strength of 8.5 T.

[b] σ_{iso} is the isotropic chemical shift ($\sigma_{\text{iso}} = \frac{1}{3}(\sigma_{33} + \sigma_{22} + \sigma_{11})$, where $|\sigma_{33} - \sigma_{\text{iso}}| > |\sigma_{11} - \sigma_{\text{iso}}| > |\sigma_{22} - \sigma_{\text{iso}}|)^{40}$.

[c] η is the asymmetry parameter ($\eta = (\sigma_{22} - \sigma_{11})/(\sigma_{33} - \sigma_{\text{iso}})$). Values were obtained with HBA simulation program.

[d] $\Delta\sigma$ is the anisotropy ($\Delta\sigma = (\sigma_{33} - (\sigma_{11} + \sigma_{22})/2$.

[e] FWHM is the full width at half maximum of the resonance.

[f] The long-range order parameter is equal to $2M - 1$, where M is the occupancy of the Te ion on the "Te" site.

(which uses the Herzfeld–Berger method (34) to exact σ_{11}, σ_{22}, and σ_{33}, the principal components of the CSA shielding tensor). The results are shown in Table 8. All the compounds except the titanium tellurates give a sharp resonance indicating that Te atom is the ordered in one site; i.e., Te is ordered within the layer.

Based on the limited number of compounds studied here, the chemical shift range for the isotropic resonance of tellurium in the $GeTeO_6^{2-}$ layer is broad, spreading from 30 to 50 ppm. The isotropic resonance of the tellurium site in $SnTeO_6^{2-}$ layer is located at higher frequency (102 ppm), while tellurium in the $TiTeO_6^{2-}$ layers resonates at a lower frequency (16.6 and -62.1 ppm). The chemical shift of ^{125}Te is also sensitive to the cation in between the layer (e.g., shifts of 50.4 ppm for Li_2GeTeO_6 and 41.7 ppm for α-Na_2GeTeO_6 are observed). Thus, the ^{125}Te NMR chemical shift is very sensitive to small changes in the local environment; consequently, any disorder should be clearly visible. Both of the spectra of Na_2TiTeO_6 and $K_{2-x}Na_xTiTeO_6$ contain one broad resonance (FWHM is large), indicating that the tellurium is disordered in these systems. There is an additional resonance (89 ppm) in the spectrum of Na_2SnTeO_6. This resonance is assigned to Te^{6+} that has substituted for Sn^{4+} on the $2a$ site. Integration of these two resonances gives a ratio of 14.6:1 leading to a composition for this compound of $Na_{1.86}Sn_{0.93}Te_{1.07}O_6$, in very good agreement with the stoichiometry determined from the Rietveld refinements of $Na_{1.84}Sn_{0.92}Te_{1.08}O_6$. The spectrum of α-Na_2GeTeO_6 contains an additional small resonance at about 30 ppm, at the same chemical shift position of β-Na_2GeTeO_6, indicating the compound contains a small amount of β-Na_2GeTeO_6. This is also consistent with the diffraction results.

The asymmetry parameter η is close to zero for all compounds, with the exception of the titanium tellurates. This indicates that all the tellurium ions are located on an axially symmetric site and provides further evidence that the Te ions are ordered within the layers. The asymmetry parameter of Na_2SnTeO_6 is approximately 0.2, which represents a slightly off axially symmetric tellurium local environment. This discrepancy between the site symmetry as determined by NMR and by crystallography is due to (dipolar) interactions of the tellurium atoms with nearby nuclei such as ^{23}Na. In cases where the CSA is small, the dipolar interactions may be dominant and lead to an error in the CSA parameters as determined from a simple simulation, which ignores these additional interactions.

Note that like the IR and Raman techniques, NMR is sensitive to local order. Since the bonding interactions within the MTeO$_6^{2-}$ layers are much stronger than those between layers, NMR will be quite sensitive to order/disorder effects within the layers but relatively insensitive to the presence of stacking faults. The combination of local order (NMR) and long-range disorder (diffraction) in compounds such as α-Na_2GeTeO_6 indicates that the disorder must result from stacking faults between layers. These stacking faults preserve the local 2D order, while destroying the 3D order. Conversely, the broad NMR and Raman lines seen for Na_2TiTeO_6 reveal significant Ti/Te disorder within the $TiTeO_6^{2-}$ layers. Thus, although Na_2TiTeO_6 and α-Na_2GeTeO_6 appear isostructural on the basis of diffraction evidence alone, further investigation reveals them to be fundamentally different from an order/disorder point of view.

The arrangement of sodium cations present in the tellurium local coordination environment in α-Na_2GeTeO_6, β-Na_2GeTeO_6, and Na_2SnTeO_6 was probed with the ^{125}Te/^{23}Na REDOR technique. The REDOR curves for each of these compounds are shown in the Fig. 9. $1 - I/I_0$ is plotted vs the evolution time, where I_0 is the intensity of the ^{125}Te resonance without ^{23}Na π irradiation and I is the intensity with ^{23}Na π irradiation. Dephasing of the Te

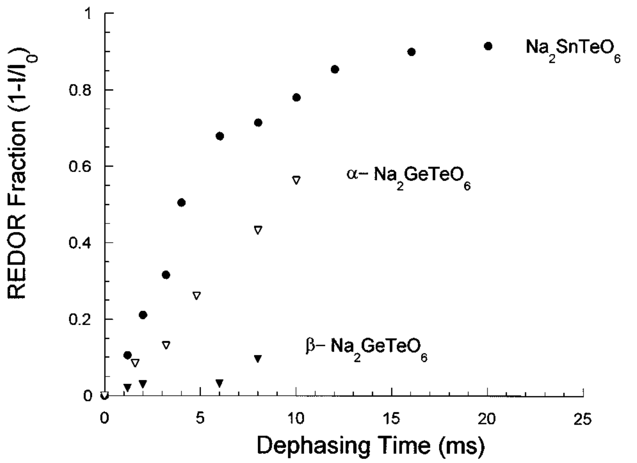

FIG. 9. The ^{125}Te/^{23}Na REDOR dephasing curves for the compounds Na_2SnTeO_6, α-Na_2GeTeO_6, and β-Na_2GeTeO_6, (solid circles, open triangles and solid triangles, respectively), obtained with a spinning speed of 9 kHz.

magnetization and thus a loss of signal at the echo will occur due to the presence of nearby Na sites. Na sites. The closer the Na–Te distance and/or the more Na nuclei nearby to Te, the stronger the dephasing of the ^{125}Te signal, resulting in a larger REDOR fraction. Figure 9 shows that the order of increased REDOR dephasing is $Na_2SnTeO_6 >$ α-$Na_2GeTeO_6 >$ β-Na_2GeTeO_6. X-ray diffraction showed that α-Na_2GeTeO_6 adopts a three-layer ilmenite structure, where each TeO_6 octahedron shares a face with one NaO_6. On the other hand, the high-temperature phase β-Na_2GeTeO_6 adopts the two-layer α-$TlSbO_3$ structure where the NaO_6 octahedra share faces exclusively with GeO_6 octahedra, so that Te–Na distances are much greater in this structure. This is consistent with the REDOR results since α-Na_2GeTeO_6 shows a more significant REDOR fraction than β-Na_2GeTeO_6. It was proposed from diffraction results that the TeO_6 octahedra share faces with two NaO_6 octahedra in Na_2SnTeO_6. The REDOR results confirm this suggestion: Na_2SnTeO_6 possesses the strongest REDOR effect of all three compounds, which is consistent with two Na atoms located adjacent to each Te atom.

DIFFaX Modeling

The NMR and Raman results of the previous sections indicate, with the exception of Na_2TiTeO_6, a high degree of cation ordering within the $MTeO_6^{2-}$ layers. However, for many of these compounds structure refinement results suggest only a partial ordering of cations. In the case of α-Na_2GeTeO_6, complete Ge/Te disorder is indicated by the refinements. The explanation that has been suggested for the apparent discrepancy is an imperfect stacking of highly ordered layers. In order to test the validity of this assumption a series of calculations using the program DIFFaX were carried out, using α-Na_2GeTeO_6 as a model compound. The program DIFFaX was written specifically for modeling diffraction patterns of compounds where disorder is introduced through stacking faults (35). Using DIFFaX, powder patterns were simulated for three possible scenarios:

1. The layer stacking is perfect, but disorder is introduced randomly within the layers.
2. The cation distribution within the layers is perfectly ordered, but stacking faults are present which interchange the Ge^{4+} and Te^{6+} positions. However, the spatial distribution of the octahedral vacancies is not disturbed by the stacking faults.
3. The cation distribution within the layers is perfectly ordered, but stacking faults are present which interchange the Ge^{4+}, Te^{6+}, and octahedral vacancies.

Inspection of the simulated powder patterns allows one to draw several general conclusions. First, those peaks that are common to the patterns of three-layer, two-layer, and one-layer compounds are insensitive to the concentration and nature of the stacking faults. They are not broadened nor is their intensity diminished by the presence of stacking faults. Furthermore, even intralayer disorder (model 1) does not seem to affect the intensity of these peaks. The most straightforward way to identify these peaks is to index the pattern with a three-layer unit cell then identify those peaks that satisfy both the rhombohedral extinction condition ($h + k + l = 3n$) and the condition that $l = 3n$. These peaks will hereafter be referred to as the invariant peaks. Considering now the remaining peaks in the powder pattern, it was found that all three models affect these peaks in slightly different ways. The presence of disorder results in a decrease in the intensity of the remaining reflections regardless of the model. The exact amount of the decrease depends upon the peak, the model, and the degree of disorder. Model 3 results in significant broadening of these peaks, whereas no broadening of these peaks was detected when using models 1 and 2 regardless of the degree of disorder. Finally, beginning from the rhombohedral ilmenite structure, both models 2 and 3 give rise to a few weak asymmetric peaks that were not obtained when using model 1. These peaks are observed, presumably, because the stacking faults violate the rhombohedral translational symmetry of the lattice. However, the strength and width of these “extra” peaks were found to depend upon not only the concentration of stacking faults, but also the distance between faults. Each of these peaks falls at a position where a peak is expected from the ordered two-layer structure (β-Na_2GeTeO_6). However, not all of the peaks in the ordered two-layer structure can be generated using a DIFFaX modeling. Inspection of the observed pattern for α-Na_2GeTeO_6, after annealing at 700°C, indicates the all of the peaks expected for a two-layer structure are present, not just those “extra” peaks generated using DIFFaX. Thus, we conclude that β-Na_2GeTeO_6 is present as a discrete phase. Furthermore, the peaks from this phase overlap with the "extra peaks" generated in DIFFaX and make them unreliable for evaluating the agreement between observed and DIFFaX simulated patterns.

Limiting our analysis to those peaks that can be indexed using the α-Na_2GeTeO_6 unit cell, we compared the DIFFaX simulated patterns to the synchrotron X-ray diffraction pattern of α-Na_2GeTeO_6. First, the peak widths of the first 23 reflections in the diffraction pattern were determined using the program PROFILE (PROFILE is a commercially available software package written by SOCABIM and is contained within the Siemens DIFFRAC AT software suite). The peak widths were plotted in a Williamson–Hall style plot (36) to look for any *hkl* dependent trends in the peak broadening. The plots revealed no statistically significant trend among different classes of *hkl* reflections, essentially eliminating model 3 from consideration. Simulated patterns were then generated for varying degrees of disorder using the first and second models. The peak intensities of the simulated patterns were determined by fitting the peaks in PROFILE and then compared to the observed peak intensities. To evaluate the quality of fit to the observed pattern, the Bragg R factor, R_B, was calculated from the formula:

$$R_B = \frac{\sum_k |I_k(\text{obs}) - I_k(\text{calc})|}{\sum_k I_k(\text{obs})}$$

Using this approach the best R_B obtained using model 1 was 3.65% for an intralayer long-range order parameter of 20% (60/40% occupancy on each metal site). The best R_B obtained with model 2 was slightly lower, 3.59%, for a completely random stacking of ordered layers. The similarity in the two values shows that diffraction techniques are essentially incapable of distinguishing intralayer disorder from a disordered stacking of ordered layers. The similarity is evident in Fig. 10, which shows the best simulated patterns obtained with each model together with the observed X-ray diffraction pattern for Na_2GeTeO_6 (700°C).

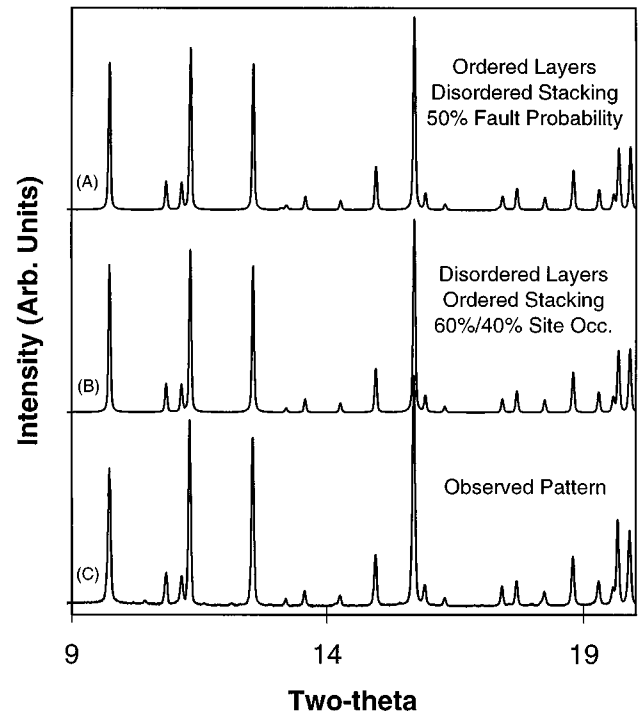

FIG. 10. The observed and DIFFaX simulated X-ray diffraction pattern of α-Na_2GeTeO_6 (700°C anneal): (a) The DIFFaX simulated powder diffraction pattern using model 2 with a 50% fault probability, (b) the DIFFaX simulated powder diffraction pattern using model 1 with a stoichiometry of $Na_2(Ge_{0.6}Te_{0.4})(Te_{0.6}Ge_{0.4})O_6$, and (c) the observed diffraction pattern.

DISCUSSION

The combined characterization results demonstrate that the order–disorder behavior in these compounds is highly anisotropic. The narrow peak widths and general similarity observed in the NMR and Raman data for all compounds containing $GeTeO_6^{2-}$ layers, α-Na_2GeTeO_6 ($R\bar{3}$), β-Na_2GeTeO_6 ($P\bar{3}1c$), Li_2GeTeO_6, $CaGeTeO_6$, $SrGeTeO_6$, and $BaGeTeO_6$, strongly suggest that these compounds contain a highy ordered distribution of germanium and tellurium within the $GeTeO_6^{2-}$ layers. However, with the exception of β-Na_2GeTeO_6 and $SrGeTeO_6$. the observation of partial Ge/Te disorder in the Rietveld refinements indicates that complete three-dimensional order is not attained. The combined experimental evidence leads to the conclusion that the disorder observed in the diffraction analysis originates from disorder in the layer stacking sesquence (which, the NMR, Raman, and IR techniques are relatively insensitive to, due to the weak ionic bonding between layers). DIFFaX modeling confirms that observed diffraction data is not inconsistent with such a hypothesis. The DIFFaX modeling also shows that the stacking faults result in an interchange of the Ge and Te sites in adjacent layers, in Li_2GeTeO_6 and α-Na_2GeTeO_6, but do not alter the rhombohedral stacking of octahedral vacancies associated with the ilmenite structure.

In contrast, the broad lines observed in the NMR and Raman data of Na_2TiTeO_6, taken together with the diffraction data, which give no evidence for Ti/Te ordering, confirm the presence of considerable disorder in the intralayer distribution of Ti^{4+} and Te^{6+}. The presence of sites with different local symmetry (due to intralayer disorder, a Te^{6+} ion could have 0, 1, 2, or 3 next-nearest tellurium neighbors within the layer) would account for the appearance of

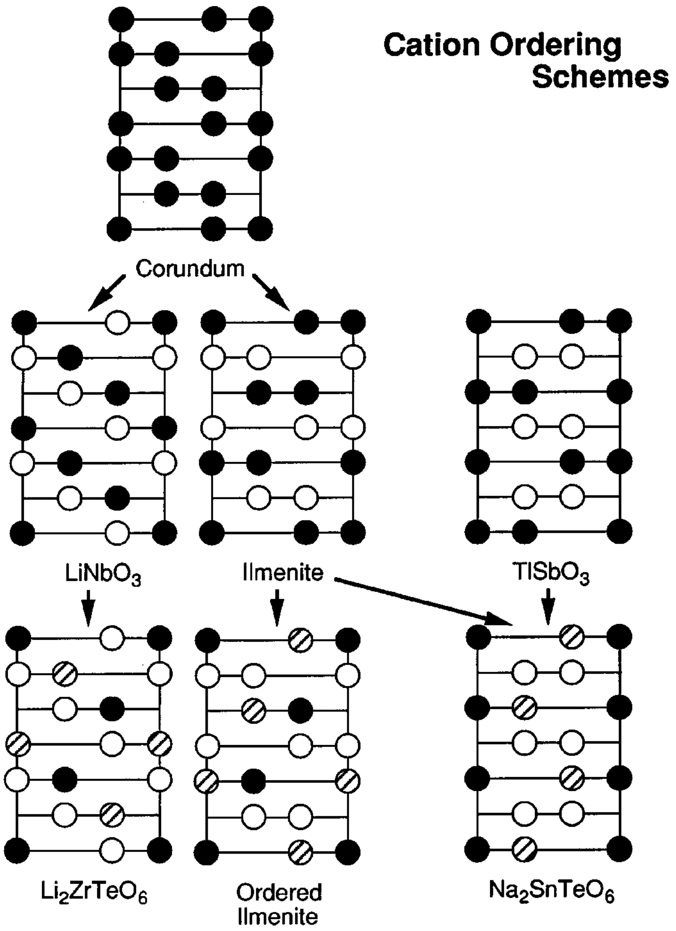

FIG. 11. Cation ordering schemes derived from M_2O_3 compounds based on hexagonal close packing of oxygen with all cations in octahedral coordination. The notation, which only shows the metal ions in each layer (at x, y positions of 0, 0, $\frac{1}{3}$, $\frac{2}{3}$, and $\frac{2}{3}$, $\frac{1}{3}$) is standard for describing such structures.

additional features in the infrared spectrum as well as several intense bands in the stretching region of the Raman spectrum. ^{125}Te NMR is also a local probe whose chemical shift is clearly very sensitive to the nature of the M^{4+} cations (e.g., the numbers of M^{4+}) in the Te local environment. A broad distribution is numbers of nearest-neighbor Ti atoms should yield a broad resonance, consistent with the observed spectrum.

Both the ordered ilmenite structure of Li_2GeTeO_6 and the structure adopted by Na_2SnTeO_6 and β-Na_2GeTeO_6 represent cation ordering arrangements that have not previously been observed. Figure 11 illustrates various known ordering arrangements for a hexagonal close packing of oxygen with two-thirds of the octahedral holes filled. The simplest member of this family is the corundum structure, where the octahedral vacancies are evenly spread throughout the lattice. If the octahedral cation sites are occupied by two distinct cations in a 1:1 ratio, they can be arranged in two possible configurations without disturbing the spatial arrangement of octahedral vacancies. The two possibilities are represented by the ilmenite and $LiNbO_3$ structures. Other cation ordering derivatives of the corundum structure such as Ni_3TeO_6 (37) and $Mn_4Nb_2O_9$ (38) are not considered here because they do not maintain a 1:1 cation ratio. Among the ilmenite and $LiNbO_3$ structures, the size difference between octahedral cations will be critical in determining which structure is the lowest energy configuration (although other possible ABO_3 structures such as perovskite may be more stable than either $LiNbO_3$ or ilmenite). If the difference in ionic radii of the two metals is large, the ilmenite structure will be more stable. As the cation size difference decreases, at some point the $LiNbO_3$ structure will become the most stable configuration. Finally, as the sizes of the two cations become very similar, a statistical distribution within the corundum structure may result. By introducing a 1:1 mixture of two different cations onto the higher valent cation site, we move from a ternary system to a quaternary system and introduce an additional ordering parameter.

The compounds Li_2ZrTeO_6 and Li_2HfTeO_6 have previously been shown to be ordered derivatives of the $LiNbO_3$ structure, but ordered derivatives of the ilmenite structure have not been previously reported. This gap in the ordering tree of the corundum family has now been filled by Li_2GeTeO_6. The structure of α-Na_2GeTeO_6 is very similar to that of Li_2GeTeO_6 on a local scale, but has a much higher concentration of stacking faults. Consideration of ionic interactions within this structure provides an explanation of why such anisotropy is observed in the cation ordering. Both M^{4+} and Te^{6+} cations share a single face of their octahedron with an A cation, resulting in A–M and A–Te distances that are quite similar in the ordered and disordered structures. Therefore, the M–Te interaction will be largely responsible for stabilization of the ordered structure. In Li_2GeTeO_6, each Te^{6+} ion has three intralayer Ge^{4+} neighbors 2.90 Å away and one interlayer neighbor 4.58 Å away. In α-Na_2GeTeO_6, these distances are 2.95 and 5.19 Å, respectively. A very crude calculation based on these distances reveals that in Li_2GeTeO_6, 88% of the total Coulombic energy gain realized by complete ordering can be achieved with a random stacking of ordered layers. In the case of α-Na_2GeTeO_6, which has a larger separation between the layers, 90% of the total ordering energy is associated strictly with intralayer ordering. This analysis neglects any contribution to the energy stabilization of the ordered state due to covalent bonding interactions, but clearly most of the energy stabilization realized upon cation ordering is associated with intralayer ordering.

The α-$TlSbO_3$ structure ($P\bar{3}1c$) has many similarities to the ilmenite and $LiNbO_3$ structures. It is also based on a hexagonal close packing of oxygens with two-thirds of the octahedral holes filled by a 1 : 1 ordered arrangement of cations. It cannot be derived from the corundum structure, however, because the distribution of octahedral vacancies is different. The individual layers are the same in the α-$TlSbO_3$ and ilmenite structures, but the two structures are differentiated by the stacking arrangement of these layers. In $NaSbO_3$ (ilmenite) all of the antimony-centered octahedra share one face with a sodium-centered octahedron. Therefore, all antimony ions are chemically and crystallographically equivalent. In α-$TlSbO_3$, half of the antimony-centered octahedra share two faces with *A*-cation-centered octahedra, while the remaining SbO_6 octahedra do not participate in face sharing. This creates two crystallographically and chemically distinct antimony sites. The presence of two nonequivalent antimony sites makes this structure is ideally suited to accommodate a further cation ordering. This situation is realized in Na_2SnTeO_6 and β-Na_2GeTeO_6.

It is interesting that Li_2GeTeO_6, β-Na_2GeTeO_6, and Na_2SnTeO_6 adopt slightly different structures. Li_2GeTeO_6 has the ordered ilmenite structure where both Ge and Te octahedra share one face with a lithium octahedron. Both β-Na_2GeTeO_6 and Na_2SnTeO_6 are ordered derivatives of the α-$TlSbO_3$ structure. In β-Na_2GeTeO_6 the lower valent germanium-centered octahedra share faces with sodium octahedra, while in Na_2SnTeO_6 the higher valent tellurium centered octahedra share faces with sodium octahedra. The first arrangement will hereafter be referred to as the $P\bar{3}1c$ structure and the second arrangement as the inverse $P\bar{3}1c$ structure. How can we understand the competition between these three structures? First, consider the coordination environment seen by the *A* cation. Figure 12 shows a view of the $SnTeO_6^{2-}$ layer in Na_2SnTeO_6. Three triangles are outlined, which represent the octahedral face associated with each of the three possible octahedral sites available for the *A* cation. In each layer, two of these sites will be filled by *A* cations while the other site will be empty. Since no metal–metal bonding is expected in these compounds, the *A* cations will tend to position themselves as far as possible from the M^{4+} and Te^{6+} cations. For this reason, in all three structures each *A* cation will have a vacancy located either directly below or directly above it and a M^{4+}/Te^{6+} cation neighbor in the other direction. Furthermore, the *A* cation will be shifted off of the center of the octahedron toward the vacancy. (In Li_2GeTeO_6, β-Na_2GeTeO_6, and Na_2SnTeO_6 this shift is 0.40, 0.41, and 0.52 Å, respectively.) If one considers only cation–cation repulsions within a purely ionic model, one would expect the *A* cation to preferentially share faces with the lower valent cation, as it does in the $P\bar{3}1c$ structure. However, such a simplistic conclusion completely neglects *A*–O interactions.

To evaluate the structural competition on a slightly more sophisticated level, Madelung energy calculations were carried out on a series of idealized structures using the program EUTAX (39). An assumption inherent to these calculations is that charge on each ion is equivalent to formal oxidation state of the ion. In highly covalent oxides this is not a very good approximation, but hopefully the ionic model can provide some insight into the competition between $P\bar{3}1c$, inverse $P\bar{3}1c$, and ordered ilmenite structures. For these calculations the lattice constants and *z* parameters of all ions were held constant, with values chosen to match the structure of β-Na_2GeTeO_6. This fixes the width of the layers and the separation of all ions in the *z* direction. The oxygen *x* and *y* values were then changed to vary and M^{4+}–O and M^{6+}–O distances, but the sum of these two distances was maintained at a constant value of 3.834 Å (i.e., $M^{4+}\text{–O} = 1.882$ Å and $M^{6+}\text{–O} = 1.952$ Å). This defines the coordinates of the $MTeO_6^{2-}$ layers. Finally, the $MTeO_6^{2-}$ layers are arranged in accordance with each of the three ordered stacking sequences and the Madelung energy is calculated. The results of this calculation are shown in Fig. 13. The positive slope in all cases can be attributed to the fact that it is energetically favorable to have oxygen closer to M^{6+} than M^{4+}. One can see that when the hexavalent cation is the same size or smaller than the tetravalent cation the $P\bar{3}1c$ structure is more stable than either the ordered ilmenite or the inverse $P\bar{3}1c$ structures. The energy difference between the three structures decreases until the M^{4+}–O distance is approximately 0.12 Å larger than the M^{6+} bond distance, at which point the energy of all three structures are degenerate. Finally, as the size of the M^{4+} cation continues to increase the inverse $P\bar{3}1c$ structure becomes the most stable configuration. The size difference between Te^{6+} and Sn^{4+}, Ti^{4+}, and Ge^{4+} are shown in Fig. 13 with dotted lines.

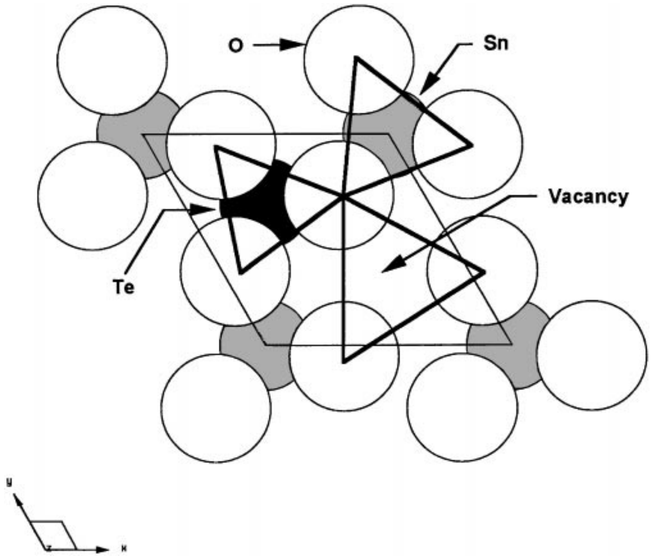

FIG. 12. A view looking down on a $SnTeO_6^{2-}$ layer. The octahedral faces which can be shared with the *A* cations, located directly above this layer, are outlined in bold. The O–O distances in these octahedral faces are 2.74 Å (Te), 3.02 Å (Sn), and 3.55 Å (Vacancy) in Na_2SnTeO_6. In β-Na_2GeTeO_6 they are 2.71 Å (Ge), 2.77 Å (Te), and 3.40 Å (Vacancy).

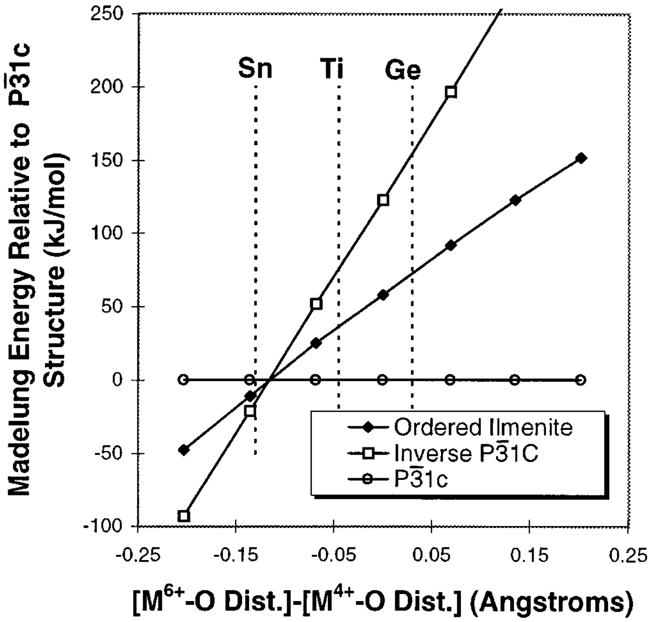

FIG. 13. The Madelung energy difference between $A_2M^{4+}M^{6+}O_6$ compounds in the three layer ordered ilmenite structure, the two layer $P\bar{3}1c$ structure (adopted by β-Na_2GeTeO_6), and the two-layer inverse $P\bar{3}1c$ structure (adopted by Na_2SnTeO_6). The more negative the energy becomes relative to the $P\bar{3}1c$ structure the more stable the structure.

We can understand the different behaviors exhibited in Fig. 13 in terms of the *A*–O interactions. Referring once again to Fig. 12, if the *A*-site cation shares faces with the larger ion, the shared octahedral face is expanded. This is undesirable for the *A* cation from a coordination point of view, because it has already shifted away from the oxygen ions in this face due to repulsion from the *M*/Te cation, and expanding the octahedral face will further increase the long *A*–O distances. Conversely, the opposite effect will hold if the *A*-site cation shares a face with the smaller ion. Thus, the *A*–O ionic interactions will be most favorable when the *A*-site cation shares faces with the smaller *M*/Te cation. In the case of Na_2GeTeO_6 the germanium ion is both smaller and lower valent, so that both Na–O attractive interactions and Na–Ge/Te repulsive interactions favor face sharing between sodium- and germanium-centered octahedra. Correspondingly, the $P\bar{3}1c$ structure is observed. In Na_2SnTeO_6 these two interactions are in competition. The Madelung energy calculations indicate that the size difference between Sn^{4+} and Te^{6+} is sufficient so that the energy gain realized from the enhanced Na–O interactions in the inverse $P\bar{3}1c$ structure is slightly larger than the energy cost of pairing sodium with the higher valent tellurium. In reality, the charge difference between the tin and tellurium sites will be smaller than two, decreasing the magnitude of the cation–cation repulsion term, but the Na–O interactions will still be highly ionic. Thus, the calculations represent a worst case scenario for the stability of the inverse $P\bar{3}1c$ structure. In light of these results it is not surprising that Na_2SnTeO_6 adopts the inverse $P\bar{3}1c$ structure.

CONCLUSIONS

Five new compounds in the $A_xM\text{TeO}_6$ family have been synthesized and structurally characterized using X-ray and neutron powder diffraction, ^{125}Te MAS–NMR (including CSA simulation and ^{125}Te/^{23}Na REDOR technique), and infrared and Raman spectroscopy. All compounds have trigonal $M\text{TeO}_6^{2-}$ layers as a common structural unit. Among the layered structures cation ordering is very high within individual layers when $M = \text{Ge}^{4+}$ or Sn^{4+}, but considerable variations exist in the coherence and configuration of the layer stacking. When $M = \text{Ti}^{4+}$, Ti/Te disorder within the layers is observed. $SrGeTeO_6$ adopts a structure with the strontium ion occupying the octahedral site directly between octahedral vacancies in the $GeTeO_6^{2-}$ layers so that no octahedral face sharing is present. The germanium and tellurium ions are ordered in all three dimensions, and the stacking of $GeTeO_6^{2-}$ layers is such that the unit cell contains only a single layer. $BaGeTeO_6$ has a similar structure with barium in trigonal prismatic rather than octahedral coordination. Ordered derivatives of the ilmenite and α-$TlSbO_3$ structures have been prepared for the first time. Madelung energy calculations help explain the structural preferences of these compounds. Both the charge and size of the *M* cation (with respect to the Te^{6+} and *A* cations) were found to play a critical role in determining the lowest energy structure of each compound. All attempts to ion exchange K^+ for Na^+ and maintain the integrity of the $M\text{TeO}_6^{2-}$ layers were unsuccessful. ^{125}Te MAS–NMR is sensitive to the local environment of tellurium atom. The presence of cation ordering within the layers is readily determined from the line width of the ^{125}Te resonance. By using ^{125}Te/^{23}Na REDOR experiment, the ordering of Sn^{4+} and Te^{6+} sites has been successfully determined in Na_2SnTeO_6, a system where diffraction cannot directly distinguish between Sn and Te due to their similar scattering factors.

ACKNOWLEDGMENTS

This work was supported by NSF Grant DMR-9308530. Synchrotron X-ray diffraction data were collected at the National Synchrotron Light Source, Brookhaven National Laboratory, which is supported by the Division of Materials Sciences, U.S. Department of Energy, under Contract DE-AC02-98CH10886. The NSLS is supported by the U.S. Department of Energy, Division of Materials Sciences and Division of Chemical Sciences. We thank Dr. David Cox for advice and assistance in the collection of the synchrotron X-ray diffraction spectra, and Dr. Brett Hunter at ANSTO for collection of neutron diffraction data for Na_2TiTeO_6 and Na_2SnTeO_6. We acknowledge the support of the National Institute of Standards and Technology, U.S. Department of Commerce, in providing neutron research facilities for Na_2GeTeO_6. We also thank Paul Schields for helpful discussions regarding the DIFFaX modeling. We express a special thanks to Dr. René Rodriguez and the chemistry department of Idaho State University for use of the Raman spectrometer and assistance in the collection of Raman spectra.

REFERENCES

1. P. Lacorre, M. Hervieu, and B. Raveau, *Mater. Res. Bull.* **19,** 693 (1984).
2. B. Wang, S. C. Chen, and M. Greenblatt, *J. Solid State Chem.* **108,** 184 (1994).
3. P. Spiegelberg, *Ark. Kemi. Mineral. Geol.* **14A** (5), 1 (1940).
4. J. B. Goodenough and J. A. Kafalas, *J. Solid State Chem.* **6,** 493 (1973).
5. H. Y. P. Hong, J. A. Kafalas, and J. B. Goodenough, *J. Solid State Chem.* **9,** 345 (1974).
6. N. Schrewelius, *Z. Anorg. Allg. Chem.* **238,** 241 (1938).
7. Y. Piffard, M. Dion, and M. Tournoux, *Acta Crystallogr. Sect. B* **34,** 366 (1978).
8. A. W. Sleight, *Mater. Res. Bull.* **4,** 377 (1969).
9. M. Bouchama and M. Tournoux, *Rev. Chim. Miner.* **12,** 80 (1975).
10. R. J. Hill, *J. Solid State Chem.* **71,** 12 (1987).
11. A. Magnéli, *Ark. Kemi Min. Geol.* **15B,** 1 (1941).
12. T. Stefanidis, A. Nord, and P. Kierkegaard, *Z. Kristallogr.* **173,** 313 (1985).
13. B. G. DeBoer, R. A. Young, and A. Sakthivel, *Acta Crystallogr. Sect. C* **50,** 476 (1994).
14. J. Choisnet, A. Rulmont, and P. Tarte, *J. Solid State Chem.* **82,** 272 (1989).
15. J. Choisnet, A. Rulmont, and P. Tarte, *J. Solid State Chem.* **75,** 124 (1988).
16. G. Bayer, *Fortschr. Miner.* **46,** 41 (1969).
17. M. Amarilla, M. L. Veiga, C. Pico, M. Gaitán, and A. Jerez, *Inorg. Chem.* **28,** 1701 (1989).
18. Diffraction patterns collected using flat plate sample holders with a laboratory diffractometer generally showed significant preferred orientation.
19. G. C. Smith, *Synchr. Rad. News* **4,** 24 (1991).
20. C. J. Howard, C. J. Ball, R. L. Davis, and M. M. Elcombe, *Aust. J. Phys.* **36,** 507 (1983).
21. R. A. Young, *in* "The Rietveld Method" (R. A. Young, Ed.), pp. 1–38. Oxford University Press, Oxford, 1993.
22. A. C. Larson and R. B. Von Dreele, "LANSCE." Los Alamos National Laboratory, Los Alamos, NM, 1994.
23. T. Gullion and J. Schaefer, *J. Magn. Reson.* **81,** 196 (1989).
24. T. Gullion and J. Schaefer, *Adv. Magn. Reson.* **13,** 55 (1989).
25. M. Robert and P. Tarte, *C. R. Acad. Sci. Paris* **283,** 195 (1976).
26. R. Frydrych, *Chem. Ber.* **100,** 3588 (1967).
27. R. Frydrych, *Chem. Ber.* **103,** 327 (1970).
28. D. B. Currie, W. Levason, R. D. Oldroyd, and M. T. Weller, *J. Mater. Chem.* **3,** 447 (1993).
29. H. M. Kasper, *Mater. Res. Bull.* **4,** 33–38 (1969).
30. R. Frydrych, *Chem. Ber.* **105,** 2427 (1972).
31. P. Tarte and M. Gabelica-Robert, *C. R. Acad. Sci. Pairs* **296,** 261 (1983).
32. F. Archaimbault, J. Choisnet, A. Rulmont, and P. Tarte, *Mater. Chem. Phys.* **30,** 245 (1992).
33. V. C. Farmer and A. N. Lazarev, "The Infrared Spectra of Minerals (Miner. Soc. Monograph 4)," pp. 51–68. Mineralogical Society, London, 1974.
34. J. Herzfeld and A. Berger, *J. Chem. Phys.* **73,** 6021 (1980).
35. DIFFaX software is based on an algorithm described in M. M. J. Treacy, J. M. Newsam, and M. W. Deem, *Proc. R. Soc. London A* **433,** 499 (1991).
36. S. A. Howard and K. D. Preston, *in* "Modern Powder Diffraction" (D. L. Bish and J. E. Post), pp. 217–272. Mineralogical Society of America, Washington DC., 1989.
37. R. E. Newnham and E. P. Meagher, *Mater. Res. Bull.* **2,** 549 (1967).
38. E. F. Bertaut, L. Corliss, F. Forrat, R. Aleonard, and R. Pauthenet, *J. Phys. Chem. Solids* **21,** 234 (1961).
39. M. O'Keeffe, EUTAX, Program for calculating bond valences. EMLab Software, Phoenix, AZ.
40. A.-R. Grimmer and B. Blumich, *NMR Basic Principles and Progress* **30,** 3 (1994).